Three-dimensional model of thermal-induced optical phase shifts in rotation sensing

Xuyou Li (李绪友), Weiwei Ling (凌卫伟), Yanhui Wei (魏延辉)*, and Zhenlong Xu (许振龙)

Harbin Engineering University, College of Automation, Harbin, Heilongjiang 150001, China
**Corresponding author: wyhhit@163.com*

Received May 7, 2015; accepted June 19, 2015; posted online July 23, 2015

By studying the thermal-induced phase shift mechanism of an interferometric fiber-optic gyroscope (IFOG) sensing coil, a novel generalized expression based on a three-dimensional (3D) model is proposed. Compared with the traditional pure Shupe effect model, the simulation results show that the new 3D model, including elastic strain and the elasto-optical effect, can describe the thermal effect of the coils more accurately. Experiments with temperature change rates between −40°C and 70°C are performed to verify the effectiveness of the proposed generalized expression. The results of our work can guide researchers in identifying countermeasures to reduce the thermal-induced bias error in IFOG.

OCIS codes: 060.2370, 060.2800, 050.5080, 120.5790, 140.6810.
doi: 10.3788/COL201513.090603.

As we all know, thermal-induced rate error[1] is one of major factors impairing coil performance. In order to reduce the thermal-induced rate error, much research has gone into investigating the temperature sources of the rate error and possible solutions to decrease the error[2–11]. It has been known for a long time that parameters in fiber coils such as the fiber refractive index, thermal expansion, thermal stress, and strain[12–14] will change with the variation of environment temperature. In this case the nonreciprocity effect caused by elastic strain and the elasto-optical effect[15,16] in the fiber for a high-accuracy interferometric fiber-optic gyroscope (IFOG) must be taken into account. Considering the actual structure characteristics of a fiber coil, the temperature of the coil at different points is cyclical and uneven for an IFOG working in a harsh environment. Therefore, the traditional two-dimensional (2D) thermal model[17,18] is incapable of analyzing the Shupe effect, elastic strain, and the elasto-optic effect induced by the asymmetrical temperature gradient.

To the best of our knowledge, this is first report about a three-dimensional (3D)[19] heat conduction model to more accurately describe the Shupe effect, elastic strain, and the elasto-optic effect induced by the thermal transient effect in an IFOG fiber coil. A novel generalized expression based on the 3D model which can fully describe the thermal-induced rate error for an IFOG is proposed.

Generally, a "pure Shupe effect"[20] is introduced for a description of the thermal in a Sagnac interferometer. The phase ϕ of a wave propagating in a piece with fiber of length l is

$$\phi(l) = \beta_0 n \cdot l + \beta_0 \left(\frac{\partial \mathrm{n}}{\partial T} \cdot \Delta T + n\alpha \cdot \Delta T \right) \cdot l, \quad (1)$$

where β_0 is the free-space propagation constant, n is the fiber effective index, ΔT is the temperature change, $\partial \mathrm{n}/\partial T$ is the thermo-optic coefficient, and α is the thermal expansion coefficient of the fiber. In order to evaluate the thermal transient effect, we use cylindrical coordinates to describe the quadrupolar (QAD) winding pattern, and set the fiber midpoint as the initial point ($s = 0$, where s is on behalf of the distance between from any point of the fiber to initial point)[19]. Integrating both partial waves in the Sagnac interferometer with their respective time dependency leads to the Sagnac phase[4]; the "pure Shupe effect" phase can be extended further to describe the rate error of the fiber coil

$$\Omega_{E1}(t) = \frac{n}{DL} \left(\frac{\partial n}{\partial T} + n\alpha \right) \int_{-L/2}^{L/2} \dot{T}(s,t)(L-2s)\mathrm{d}s, \quad (2)$$

where D is the average diameter of the fiber coil. However, varying the temperature could cause a change in the plication pressure between the cladding layer and the silica fiber core, which results in extrusion on the silica fiber core. Finally, the fiber length l corresponding to the elastic deformation and the fiber refractive index corresponding to the elasto-optical effect are changed[12,21]. Consequently, it is necessary to take into account the nonreciprocal phase shift which is caused by the elastic strain and the elasto-optical effect[15,22–24]. As the temperature varies, the difference in thermal expansion between the coating and glue materials of the coil is obvious. When the temperature increases or decreases, the thermal stress of the silica fiber core changes. Here, we continued taking an l length typical fiber in a fiber coil as an example. Once the fiber coil temperature varies, the pressure acting on the silica fiber core will also change. Then, the fiber length and the fiber refractive index will change because of the pressure. The phase shift with changing pressure is given as

$$\Delta\phi(l) = \beta \cdot \Delta l + l \cdot \Delta\beta = \beta l \cdot \frac{\Delta l}{l} + l \cdot \frac{\Delta\beta}{\Delta n}\Delta n. \quad (3)$$

Assuming $\beta \approx n\beta_0$, $d\beta/dn \approx \beta_0$, and $\Delta l/l \approx \varepsilon_z$, Eq. (3) can be rewritten as

$$\Delta\phi(l) = \beta_0\, l \cdot n\,\varepsilon_z + \beta_0 l \cdot \Delta n, \quad (4)$$

where ε_z is the axial strain of the fiber and, Δn is the refractive index variation of the fiber. In the fiber coil, it can be considered approximately that the thermal-induced pressure in the fiber only exists in the radial direction. According to the theory of elasticity, the change of fiber refractive index induced by thermal stress can be described as

$$\Delta n = -\frac{1}{2}n^2(P_{11}\varepsilon_x + P_{12}\varepsilon_y + P_{12}\varepsilon_z), \quad (5)$$

where P_{11} and P_{12} are the photoelastic coefficients, and ε_x, ε_y, and ε_z are the horizontal strain, vertical strain, and axial strain, respectively. The relationship between the stress and strain in three orthogonal directions is

$$\begin{bmatrix}\varepsilon_x\\ \varepsilon_y\\ \varepsilon_z\\ \varepsilon_{yz}\\ \varepsilon_{zx}\\ \varepsilon_{xy}\end{bmatrix} = \begin{bmatrix} 1/E & -v/E & -v/E & 0 & 0 & 0\\ -\nu/E & 1/E & -\nu/E & 0 & 0 & 0\\ -\nu/E & 1/E & 1/E & 0 & 0 & 0\\ 0 & 0 & 0 & 1/G & 0 & 0\\ 0 & 0 & 0 & 0 & 1/G & 0\\ 0 & 0 & 0 & 0 & 0 & 1/G\end{bmatrix}\begin{bmatrix}\sigma_x\\ \sigma_y\\ \sigma_z\\ \sigma_{yz}\\ \sigma_{zx}\\ \sigma_{xy}\end{bmatrix}, \quad (6)$$

where $\sigma_i(i = x, y, z)$ and $\sigma_j(j = yz, zx, xy)$ are the normal stress and shear stress, respectively, in three orthogonal directions; $\varepsilon_i(i = x, y, z)$ and $\varepsilon_j(j = yz, zx, xy)$ are linear strain and shear strain, respectively, in three orthogonal directions; ν is Poisson's ratio; E is modulus of elasticity; G is the shear modulus of elasticity. Varying temperature could cause a change in the placation pressure between the cladding payer and the silica fiber core. Considering that the fiber length is much longer than the fiber cross-sectional diameter of the fiber coil, the axial stress can be ignored. Furthermore, axial strain can be obtained from the horizontal stress. In a fiber coil, a typical thermal-induced pressure of the fiber core can be divided into the horizontal stress P_h and vertical stress P_v (Fig. 1), and the horizontal stress P_h and vertical stress P_v are perpendicular, which are expressed

$$\begin{bmatrix}\sigma_x\\ \sigma_y\\ \sigma_z\\ \sigma_{yz}\\ \sigma_{zx}\\ \sigma_{xy}\end{bmatrix} = \begin{bmatrix}-P_h\\ -P_v\\ 0\\ 0\\ 0\\ 0\end{bmatrix}. \quad (7)$$

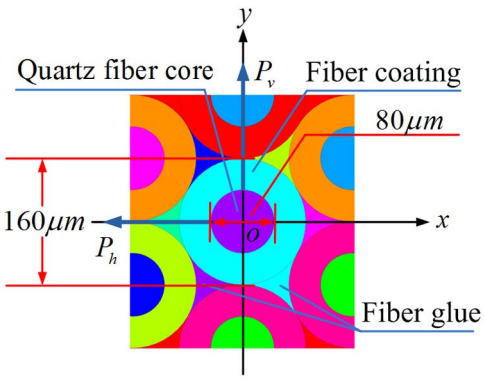

Fig. 1. Typical thermal-induced pressure of the fiber core.

Considering the thermal-induced pressure of the fiber core can be seen as uniform radial compression[14], the stress can be rewritten as

$$P(T) = P_h = P_v. \quad (8)$$

Therefore, by integrating Eqs. (3)–(8), the change in phase shift caused by changing thermal-induced pressure is obtained

$$\Delta\varphi(l) = \beta_0\left\{\frac{2\nu n}{E}\Delta P(T) + \frac{n^3}{2E}[(1-\nu) \cdot p_{11} + (1-3\nu) \cdot p_{12}]\Delta P(T)\right\}l, \quad (9)$$

where $\Delta P(T) = P(T_t) - P(T_0)$. Using the approach given by Mohr[4], the result can be extended further to describe the rate error

$$\Omega_{E2}(t) = \frac{n}{DL}\left\{\frac{2\nu}{E} + \frac{n^2}{2E}[(1-\nu) \cdot p_{11} + (1-3\nu) \cdot p_{12}]\right\} \times \int_{-L/2}^{L/2}\dot{P}(T(s,t))(L-2s)\mathrm{d}s, \quad (10)$$

where the term inside the first brace bracket relates the rate error with thermal stress, and the term inside the second bracket is the expression of thermal stress induced by fiber coating expansion. We finally obtain the total thermal-induced rate error $\Omega_E(t)$ for the IFOG as the summation of $\Omega_{E1}(t)$ and $\Omega_{E2}(t)$

$$\Omega_E(t) = \Omega_{E1}(t) + \Omega_{E2}(t). \quad (11)$$

In order to calculate the total thermal-induced rate error $\Omega_E(t)$ quantitatively, we must discretize the coil. By using the approach given by Li[19], we finally obtain a numerical expression

$$
\begin{aligned}
&\boldsymbol{\Omega}_E(t,T)\\
&=\frac{2n}{DL}\left(\frac{\partial n}{\partial T}+n\alpha(T)\right)\sum_{i}^{N_{ccw}} r_i\int_0^{2\pi}\dot{T}|_{(r_i,\theta,z_i,t)}(r_i\theta+s_{i0})\mathrm{d}\theta\\
&+\frac{2n}{DL}\left(\frac{\partial n}{\partial T}+n\alpha(T)\right)\sum_{j}^{N_{cw}} r_j\int_0^{2\pi}\dot{T}|_{(r_j,\theta,z_j,t)}(r_j\theta-s_{j0})\mathrm{d}\theta\\
&+\frac{2n}{DL}\left\{\frac{2\nu}{E}+\frac{n^2}{2E}[(1-\nu)\cdot p_{11}+(1-3\nu)\cdot p_{12}]\right\}\\
&\times\sum_{i}^{N_{ccw}} r_i\int_0^{2\pi}\dot{P}|_{(r_i,\theta,z_i,t)}(r_i\theta+s_{i0})\mathrm{d}\theta\\
&+\frac{2n}{DL}\left\{\frac{2\nu}{E}+\frac{n^2}{2E}[(1-\nu)\cdot p_{11}+(1-3\nu)\cdot p_{12}]\right\}\\
&\times\sum_{j}^{N_{cw}} r_j\int_0^{2\pi}\dot{P}|_{(r_j,\theta,z_j,t)}(r_j\theta-s_{j0})\mathrm{d}\theta, \qquad (12)
\end{aligned}
$$

where r_i, r_j, z_i, z_j, s_{i0}, s_{j0}, and θ are the fiber coil parameters; $\dot{T}|(r_i,\theta,z_i,t)$ and $\dot{T}|(r_j,\theta,z_j,t)$ denote the temperature change relative to the initial temperature distribution along the ith or jth turn; the terms $\dot{P}|(r_i,\theta,z_i,t)$ and $\dot{P}|(r_j,\theta,z_j,t)$ denote the thermal-induced stress with the initial stress distribution along the ith or jth turn.

Simulation by using the finite-element method (FEM) is performed to obtain the thermal-induced rate error of the IFOG based on our 3D model. Parameters describing the characteristics of the fiber coil with a QAD winding pattern are listed in Table 1. The thermal parameters and thermal stress physical parameters are provided in Table 2. Some temperature-dependent physical parameters are provided in Table 3[19,22]. In Table 2, the Al alloy material is used to produce a spool for wrapping up the fiber coil.

In order to verify the correctness of the 3D model, two experimental schemes are proposed. In the first scheme, the temperature excitation of boundary of the 3D model starts at 20°C and varies between 20°C and 70°C, as shown by the blue dash–dot line in Fig. 2(a). To make our experimental scheme more persuasive, three different temperatures change rates of 0.5°C/min, 1°C/min, and 2°C/min are used. The temperature will hold for 10 min at temperature points 20°C, 30°C, 40°C, 50°C, 60°C, and 70°C. The second experimental scheme is a repeat experiment. In the second experimental scheme, the temperature excitation starts at 20°C holding for 30 min, and sits at −40°C and 60°C for 1 h. The temperature change rate is 1°C/min, and is repeated 3 times at same time frame in 3 days as shown by the blue dash–dot line in Fig. 2(b). The fiber coil with housing used in the simulation is shown in Fig. 3(a).

Table 1. Parameters of the Fiber Coil

Parameters	Values
Length of the Fiber Coil L (m)	998
Outer Radius R_{out} of the Fiber Coil (cm)	6.05
Inner Radius R_{in} of the Fiber Coil (cm)	5.5
Coil Height H (cm)	1.3
Number of Winding Layers M	40
Number of Loops per Layer N	68
Effective Index of Fiber Core n	1.44
Thermo-optic Coefficient $\partial n/\partial T$	1.0×10^{-5}
Photoelastic Coefficients P_{11} and P_{12}	0.121 and 0.270

Table 2. Parameters for Calculation

Parameters	Al Alloy	Core	Coating	Glue
Density ρ (kg/m^3)	2740	2203	1190	970
Specific heat c (J/(kg · K))	896	703	1400	1600
Thermal conductivity λ (W/(m · K))	221	1.38	0.21	0.21
Poisson's ratio ν	0.35	0.186	0.4	0.499
Young's modulus (GPa)	70	76		
Coefficient α (K^{-1})	2.3×10^{-5}	5.5×10^{-7}		

Based on the theoretical analysis, the aforementioned material parameters, and the aforementioned simulation conditions, the simulation results are shown in Fig. 4. Figure 4 show the rate error $\boldsymbol{\Omega}_{E1}$ (red dash–dot line), $\boldsymbol{\Omega}_{E2}$ (black dotted line), and total $\boldsymbol{\Omega}_E$ (blue solid line). Figure 4 clearly shows that the rate error $\boldsymbol{\Omega}_{E2}$ caused by elastic strain and the elasto-optical effect is very heavily dependent on the total thermal-induced rate error; consequently, it cannot be neglected when the temperature varies.

In order to verify the correctness of the simulation, experiments with a QAD fiber coil are performed and the temperature is controlled according to the red solid line shown in Fig. 2. To ensure the experimental accuracy, the IFOG is divided into two parts: the fiber coils with housing [Fig. 3(b)] are placed into a temperature test chamber and other parts are placed into an incubator. Thirteen temperature sensors are mounted evenly on four surfaces of the housing. Although the temperatures on the surfaces of the housing are different, the differences are minor and neglected in our experimental work. Consequently, only one testing temperature value was plot in Fig. 2 (the blue dash–dot line).

To eliminate the influence of noise, the output signal is processed by subtracting the mean value of the signal from the original, as plotted in Fig. 5 with a black dash–dot line, whereas the blue solid line is the total $\boldsymbol{\Omega}_E$ rate error based on our 3D model. As the experimental results shown in Fig. 5, the experimental values show much agreement

Table 3. Parameters of the Coating Material and Glue Material for our Optical Fiber at Different Temperatures

T (°C)	Young's Modulus E_{coating} (GPa)	Thermal Expansion Coefficient α_{coating} (1/K)	Young's Modulus E_{glue} (MPa)	Thermal Expansion Coefficient α_{glue} (1/K)
−40	1.820	5×10^{-5}	85	1.5×10^{-4}
−20	1.66	5×10^{-5}	22	2×10^{-4}
0	1.622	5×10^{-5}	6	2.3×10^{-4}
20	1.585	7×10^{-5}	1	2.3×10^{-4}
40	1.259	1.2×10^{-4}	1	2.3×10^{-4}
60	0.794	1.5×10^{-4}	1	2.3×10^{-4}

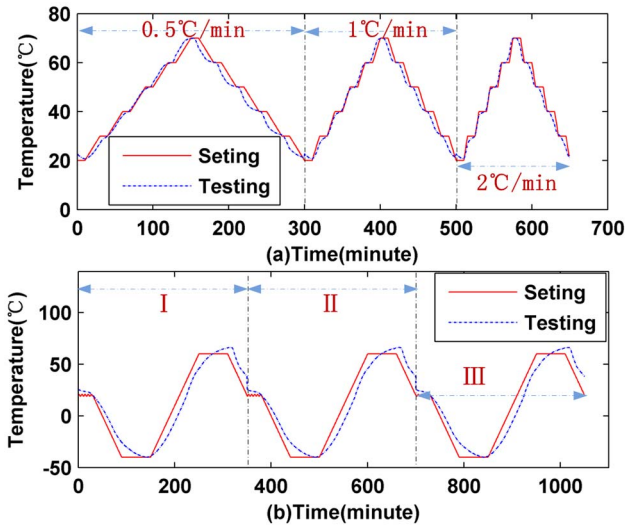

Fig. 2. Setting (red solid line) and testing (blue dashed line) temperature: (a) first temperature load scheme and (b) second temperature load scheme.

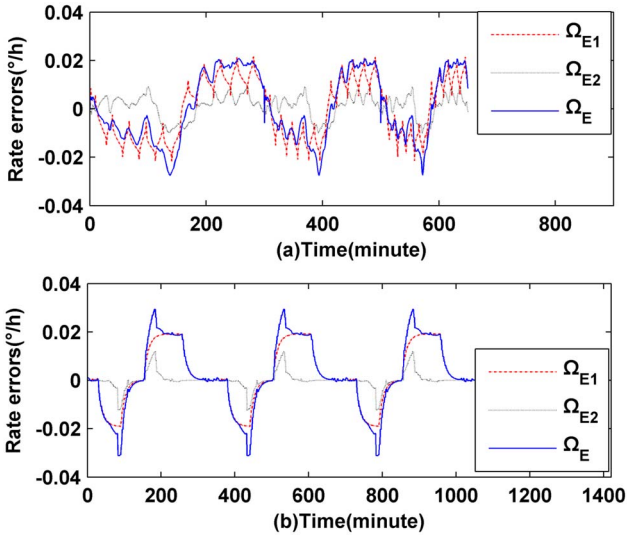

Fig. 4. Calculation of rate error Ω_{E1} (red dash–dot line), Ω_{E2} (black dotted line), and Ω_E (blue solid line): (a) first simulation and (b) second simulation.

with the simulation values, which further verifies our 3D model. The reason that underlies the differences between the experimental values and simulation values (Fig. 5) may be the nonideal QAD winding in the fabrication of the fiber coil and the ideality of our model.

In conclusion, we present a novel generalized expression based on a 3D model that can accurately describe the thermal-induced rate error in the IFOG. As can be seen

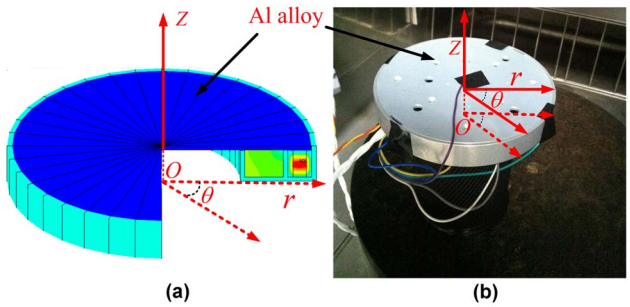

Fig. 3. Fiber coil and housing: (a) simulation profile and (b) experimental environment diagram.

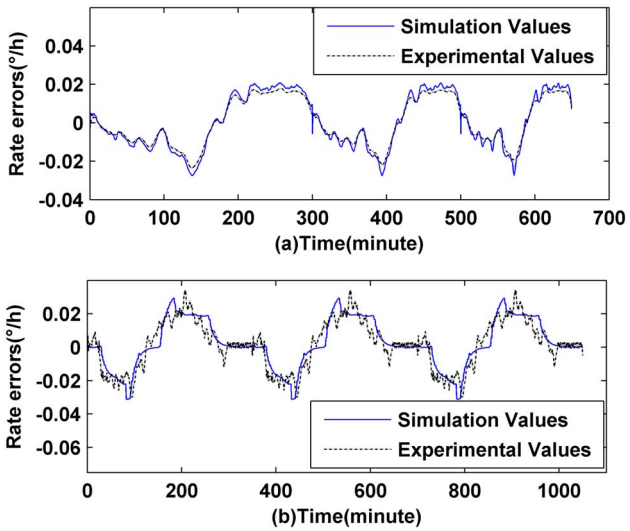

Fig. 5. Rate errors of IFOG in simulation (blue solid line) and experiment (black dash–dot line): (a) first experiment and (b) second experiment.

from our simulation and experiments, the experimental results show much agreement with the simulation values, which verifies our analysis results that the thermal stress factors of the fiber coil cannot be neglected. The successful design of the 3D model will helpful for researchers to optimize thermal design in the manufacture of IFOG.

This work was supported by the National Natural Science Foundation of China (No. 51205074), the Specialized Research Fund for the Doctoral Program of Higher Education of China (No. 20112304120007), and the Harbin Specialized Research Foundation for Innovation Talents (No. RC2012QN009037).

References

1. D. M. Shupe, Appl. Opt. **19**, 654 (1980).
2. D. W. Zhang, Y. X. Zhao, W. L. Fu, W. Q. Zhou, C. Liu, X. W. Shu, and S. L. Che, Opt. Lett. **39**, 1382 (2014).
3. N. J. Frigo, Proc. SPIE **0412**, 268 (1983).
4. F. Mohr, J. Lightwave Technol. **14**, 27 (1996).
5. J. Blake, B. Szafraniec, and J. Feth, Opt. Lett. **21**, 1192 (1996).
6. I. Golub and H. Exir, Opt. Lett. **38**, 1536 (2013).
7. S. Knudsen and K. Bløtekjær, Opt. Lett. **20**, 1432 (1995).
8. Z. H. Li, Z. Meng, T. G. Liu, and X. S. Yao, Opt. Express **21**, 2521 (2013).
9. Z. X. Gao, Y. G. Zhang, G. C. Wang, and W. Gao, Opt. Eng. **53**, 016114 (2014).
10. S. S. Du, Y. M. Guan, J. Jin, and C. X. Zhang, Optik **123**, 748 (2012).
11. H. Liu, W. Wang, X. Li, and F. Gao, Chin. Opt. Lett. **11**, 101501 (2013).
12. K. Brugger, Appl. Opt. **10**, 437 (1971).
13. Y. C. Yang, Opt. Eng. **40**, 2107 (2001).
14. F. E. Seraji and G. Toutian, Prog. Quantum Electron. **30**, 317 (2006).
15. S. C. Her and C. Y. Huang, Sensors–Basel **13**, 1846 (2013).
16. F. Mohr and F. Schadt, in *Proceedings of Computational Technologies in Electrical and Electronics Engineering, IEEE Region 8 International Conference* 372 (2008).
17. O. F. Tirat and J. M. Euverte, Proc. SPIE **2837**, 230 (1996).
18. Y. G. Zhang, Z. X. Gao, G. C. Wang, and W. Gao, IEEE Photon. Technol. Lett. **26**, 18 (2014).
19. M. C. Li, T. G. Liu, Y. W. Zhou, J. F. Jiang, L. L. Hou, J. J. Wang, and X. S. Yao, Proc. SPIE **6830**, 68300E (2007).
20. F. Mohr and F. Schadt, Proc. SPIE **5502**, 410 (2004).
21. N. Lagakos, J. A. Bucaro, and J. Jarzynski, Appl. Opt. **20**, 2305 (1981).
22. M. Webber, R. Willig, H. Raczkowski, and A. Dineen, J. Lightwave Technol. **30**, 2356 (2012).
23. C. Li, C. Zhang, N. Song, and H. Xu, Chin. Opt. Lett. **9**, 020604 (2011).
24. T. Qin, Z. Li, C. Wu, and Z. Wang, Chin. Opt. Lett. **12**, S20602 (2014).